Mass Transfer and Chemical Reactions in Bubble Swarms with Dynamic Interfaces

Athanas Koynov and Johannes G. Khinast
Dept. of Chemical and Biochemical Engineering, Rutgers University, Piscataway, NJ 08845

Grétar Tryggvason
Dept. of Mechanical Engineering, Worcester Polytechnic Institute, Worcester, MA 01609

DOI 10.1002/aic.10529
Published online July 18, 2005 in Wiley InterScience (www.interscience.wiley.com).

Detailed, high-resolution numerical simulations have been performed on the buoyancy-driven motion of deformable, chemically reacting bubbles for different operating conditions, that is, Weber, Morton, and Schmidt numbers. In our simulations different bubble shapes and types of bubble wakes were observed. The wake types range from a closed wake without recirculation, to a closed wake with recirculation, to an unsteady wake, leading to vortex-shedding wakes. Two different bubble-rise trajectories were observed for different conditions: straight and zigzag shaped. The mass-transfer rates and the yields and selectivities of liquid-phase chemical reactions were determined for each case. A detailed analysis of the results was carried out, relating the differences in chemical reaction efficiencies to the dynamics of each flow. Furthermore, to obtain a better understanding of the dynamics of the flows inside bubble swarms and their impact on chemical reactions, numerical simulations were performed of multiple bubbles rising in a swarm. Different bubble counts, geometric configurations, and size distributions were considered. Mass-transfer rates and chemical reaction selectivities were determined and a comparison is presented between the results for bubble swarms and single bubbles. It was shown that for mixing-sensitive reaction networks, the hydrodynamics of the bubble swarm may significantly impact the reaction selectivity. Furthermore, it was demonstrated that bubble swarm dynamics differ from the dynamics of single bubbles. © 2005 American Institute of Chemical Engineers *AIChE J,* 51: 2786–2800, 2005
Keywords: deformable bubbles, bubble swarms, chemical reactions, mass transfer, selectivity

Introduction

Many important industrial chemical processes and naturally occurring phenomena involve chemical reactions between two fluid phases, that is, between two immiscible liquids or a gas and liquid, where one of the phases is dispersed and the other one forms a continuum. In most cases, a reactant from one phase is transported into the second phase, where it reacts with another reactant to form products, which can remain in this phase or transfer back in the original one. Depending on the specifics of these multiphase chemical processes (such as reaction rates, solubilities, vapor pressures of products) different multiphase reactors such as bubble columns, spray towers, fluidized beds, or stirred vessels, are used.

Significant efforts have been devoted to the understanding of reactor dynamics and scale-up, and to the modeling of multiphase reactors. Most studies were aimed at the macroscale (such as the large-scale mixing patterns in a reactor) or at

Correspondence concerning this article should be addressed to J. G. Khinast at khinast@rutgers.edu.

© 2005 American Institute of Chemical Engineers

simplified and idealized reactor models, such as CSTR or axial dispersion models. This top-down approach has significantly improved our understanding of complex multiphase processes. For many systems, however, this is not satisfactory. Microscale phenomena may become decisive for a process, such as when fast multiphase reactions are carried out, which are known to be mixing sensitive. In this case, the micromixing, that is, the microscale fluid dynamics, determines the selectivity of the chemical process, as shown recently in an experimental study by our group.[1] For several years our group has focused on a bottom-up strategy, where we try to understand the phenomena on a small scale, by studying chemical reactions close to single or multiple bubbles or droplets.[2,3] In this article we report significant progress of our efforts: we are now able to carry out direct numerical simulations (DNS) of chemically reacting bubble/droplet swarms with deformable interfaces, which enables us to study a wide variety of microscale phenomena.

In this work we focus on gas–liquid reaction systems, where the liquid phase is the continuous one, as encountered in bubble column reactors (BCRs) operated in the bubbly or vortical-spiral flow regime (that is, for low superficial gas velocities typically below 10 cm/s). During bubble column operation, gas is sparged at the bottom of the column and the resulting buoyancy-driven flow causes circulation and gas–liquid mixing. Depending on the operating conditions, the bubbles have a wide variety of different shapes and sizes, and typically there are significant interactions between the individual bubbles. Bubbly flows are the contacting scheme of choice for many industrial processes, such as oxidations and fermentations.[4,5] The strongly turbulent flow regimes obtained at higher superficial gas velocities, where individual bubbles cease to exist, are currently beyond our capabilities.

The focus of this report is a detailed description of the reactions occurring in deformable bubble swarms by using DNS of the multiphase fluid dynamics, mass transfer and transport, and of the chemical reactions. To the best of our knowledge, we are the first group to report such a study. In the next section background information on bubble reactors, bubble swarms, mixing and chemical reactions, modeling, and experimental studies is presented, followed by a section on the modeling of the system. Readers not interested in the modeling may skip this section together with the fourth section on the numerical approach. Results, conclusions, and future directions of our work are presented in the final sections.

Background

From the literature, it is well known that the transport of chemical species in a reactive system with multiple reactions may have impact on the product distribution. Because transport phenomena can have a significant impact on the efficiency of a chemical reactor, a detailed understanding of these processes can be crucial for optimal design and operation. This was first reported in the 1950s.[6-8] Since then much research has been devoted to the subject of mixing in different systems,[9-11] including multiphase flows[2,3,12,13] that are the focus of this work.

Gas–liquid chemical reactors, such as BCRs, have been studied extensively, both experimentally and numerically. However, because of the complex multiphase hydrodynamics, there is still a lack of a fundamental understanding of their dynamics. Because direct numerical simulations of BCRs are still computationally infeasible, two main approaches have been adopted.

The first approach focuses on the large-scale mixing patterns and dynamics of the reactor. Reactor design, scale-up, hydrodynamics, and mass-transfer correlations have been reviewed by many authors.[4,5,14-20] Although these studies were based mainly on experimental work in small-scale laboratory columns, in recent years it has become computationally possible to simulate the reactor hydrodynamics using two-dimensional (2D) and three-dimensional (3D) Euler–Euler or Euler–Lagrange models, with the main advantage being their applicability to large-scale, industrially sized reactors (provided that sufficient resolution of the computational grid can be achieved). Euler–Lagrange models describe the liquid phase as a continuum and track each individual bubble as a point source (that is, without resolving its interface) as it rises because of buoyancy.[21-24] In contrast, Euler–Euler models represent the two phases as interpenetrating continua.[25-28] The results of either one of these hydrodynamic simulations can be used to study mixing in the reactor and to predict the conversion, yield, and selectivity toward the different reaction products.

By design, Euler–Euler and Euler–Lagrange models can generate only a coarse-grid representation of the flow in the reactor because computational limitations prohibit resolution down to the Kolmogorov or Batchelor scale. Only meso- and macroscale features of the flow field can be captured. Thus, reactive mixing computations based on these models are valid, provided that characteristic reaction times be of the order of the meso- and macromixing timescales in the reactor. However, fast reactions require resolution of the flow field on the microscale,[13,29,30] and subgrid closures that augment the coarse-scale models[31] are required.

The second approach takes the opposite route and focuses on the dynamics and the direct resolution of the flow of single bubbles. The knowledge of the single-bubble behavior can then be used to extrapolate to reactor-scale flows. In many numerical studies the bubble shape is assumed to be constant. Aris[32] studied the gas–liquid mass transfer during the steady ascending motion of small spherical bubbles. Legendre and Magnaudet[33] investigated the mass and heat transfer from a spherical bubble in accelerated flows. These studies were recently extended by the research group of Khinast[2,3,30] to the case of reacting, nonspherical (elliptical) bubbles with perfect-slip boundaries, and included an investigation of the effects of the wake dynamics on the liquid-phase mass transport and chemical reactions. It was demonstrated that the behavior of the flow around nonspherical bubbles can change radically, leading to differences in chemical reaction selectivities. The main limitations of these studies, which are relaxed in this paper, were

(1) the focus on a single bubble, vs. a bubble swarm
(2) the assumption of a rigid bubble

In real bubble flows, there are interactions between bubbles, as well as a coupling between the bubble shape and the liquid-phase hydrodynamics. The latter can cause a bubble's shape to change significantly under the effect of the hydrodynamic forces. These changes, in turn, can affect the hydrodynamics of the flow around the bubble and consequently the gas–liquid mass-transfer and the liquid-phase transport.

Even though DNS of reactor-scale flows is currently unfeasible (because of the large number of bubbles, which need to be considered and the large dimensions of the physical domains),

advances are being made toward the multiscale modeling of such flows.[34] Deen et al.[34] used DNS of the hydrodynamics of bubble motion on a small scale (based on methods similar to those described in this paper) to obtain closure information for models used at the large scale (such as Euler–Lagrange).

Experimental investigations of single-bubble flows were usually based on variations of image analysis and particle image velocimetry (PIV) techniques. A typical example is the work of Tokuhiro et al.,[35]which examines the flow past an oscillating bubble using a combination of PIV and an infrared shadow technique to resolve both the liquid-phase velocity field and the bubble contour. Lage and Esposito[36] used photographic techniques to measure bubble sizes, and Raymond and Rosant[37] used imaging methods to investigate the dependency of the aspect ratio of nonspherical bubbles on the physical properties of the multiphase system. Choi et al.[38] implemented a combination of flow-visualization techniques and PIV to provide an in-depth look at the motion of deformable gas bubbles in a stagnant liquid. Recently, significant progress has been made by Bork and coworkers, who applied image analysis and fluorescence methods to study the flow dynamics and mass transfer from single bubbles.[39,40]

On the numerical front, several different techniques have been applied to the modeling of flows with deformable interfaces. In the first approach, the front is captured directly on a uniform grid, with the marker and cell (MAC) method and the volume of fluid (VOF) method being the prime examples. In these methods, the flow is solved for on a single grid with the two phases being identified by marker particles and marker functions. These methods are widely used[41,42] despite the difficulties associated with accurately defining the interface and computing surface tension and mass transfer. Recently, Bothe et al.[43] performed VOF-based numerical simulations of the mass transfer of a gas from deformable bubbles and bubble chains. Lagrangian methods,[44] in which the grid follows the fluid, have provided useful insight into the mechanisms of the deformation of bubbles. Another class of methods, where separate fitted grids are used for each phase,[45,46] can provide a very high accuracy for simple geometries, but are usually inapplicable for flows with unsteadily evolving interfaces. In front-tracking methods a separate, deformable grid is used to track the interface, whereas the flow is computed on a fixed uniform grid.[47-49] In this work the method developed by Tryggvason is used to study bubble swarms and interactions.

Because of the intricacy of bubble interactions in bubble swarms (such as wake synchronization, coalescence, and breakup), the dynamics of these swarms are highly complicated, and many problems remain unresolved. The intensity of interactions strongly depends on the system parameters, such as bubble size distribution and bubble holdup. Reese and Fan[50] reported a uniform bubble size distribution and insignificant bubble–bubble interactions for low gas void fractions. Other authors observed that the bubble shape and trajectory in bubble swarms depend on the gas holdup[51,52] and concluded that the slip velocity in bubble swarms is higher than that of a free-rising bubble.[52] Bubble-wake interactions, bubble breakup, and coalescence were studied by many research groups.[53-56]

Bubble-wake dynamics primarily influence the path of a rising bubble. However, the wake dynamics also play a major role in bubble–bubble interactions. The interaction of bubble-wake structures results in either synchronization of the flow or in trailing bubble paths. These interactions occur between a leading bubble and a trailing bubble, whereby the latter is captured in the wake, where it can experience jumps of several bubble diameters. These jumps are caused by the periodic vortex shedding of the leading bubble and the induced upward flow. During this period, the bubble motion is not continuous because the bubble is alternately accelerated and decelerated. Whether the bubble is repelled or remains in the wake until collision occurs depends on the time within the shedding cycle and the location at which the trailing bubble laterally approaches the wake of the leading one. Single bubbles and bubbles in swarms behave quite differently. For example, small bubbles become irregularly shaped like larger single bubbles as the result of the different hydrodynamics in the bubble swarm.[57] Unlike single bubbles, bubbles in a swarm disturb each other, resulting in a nonellipsoidal shape and a more racked trajectory, which induces a higher rising velocity.

Bubble and drop coalescence has been studied by many groups, both numerically and experimentally. Most bubbles coalesce by a trailing bubble "bumping" into a leading one, that is, there is an alignment of the trailing bubble, followed by acceleration and elongation.[58] Upon impact, a flattening of the contacting bubble surfaces occurs, leaving a thin liquid film, which is typically 1 to 10 μm in thickness. The film drains until it is only several nanometers in thickness, leading to coalescence. Coalescence occurs only if the two bubbles are in contact longer than required for the film to drain. Once the critical thickness is reached, an instability mechanism causes instantaneous film rupture and formation of a coalesced bubble. The entire process occurs on a timescale of milliseconds, the rate-determining step being film drainage.[59] Bubble breakup is caused by several effects. Breakup in the absence of free-stream disturbances is believed to be attributable to Rayleigh–Taylor or Kelvin–Helmholtz instabilities,[60,61] which are the result of the interface between two liquids being unstable to perturbations of wavelengths of a critical value, if the upper fluid has higher density than that of the lower one. Another breakup mechanism, especially at higher pressures, is a centrifugal force inside the bubble caused by a Hill's vortex (internal rotation). In the presence of disturbances, turbulence, or liquid-phase shear, breakup can occur for significantly smaller bubble sizes (for drops see, for example, Bentley and Leal[62] or Tsouris and Tavlarides[63]). In this work, we choose not to allow for bubble breakup and coalescence, although we will include it in future work.

Problem Formulation

A 2D front-tracking/front-capturing hybrid method by Tryggvason et al.[48] is used to simulate the motion of deformable gas bubbles in a continuous liquid. The choice of 2D resolution was based on the need for sufficient grid resolution, which would have been unattainable in 3D using current computational technology. As a consequence we cannot capture spiraling trajectories and the ensuing vortical structures in the bubble wakes. For many systems, however, in which bubbles rise in nearly 2D zigzag trajectories, the method discussed herein will provide adequate representation of the bubble behavior. This proposition can be confirmed through the agreement of the simulation results with experimental data obtained by other research groups.[64] In our method, a single set of conservation

equations is solved on a 2D fixed grid. The gas–liquid interface is tracked using a second, one-dimensional moving grid. The material properties of the fluid change across the grid, to represent gas and liquid, respectively. A detailed description of the method and a comparison to other methods currently used for the simulation of multiphase flows can be found in Tryggvason et al.[48] In our work, their method was augmented to include gas–liquid mass transfer as well as liquid-phase mass transport and chemical reactions. Systems with different fluid properties, operating conditions, and number of bubbles were simulated to obtain a better understanding of the local dynamics in bubble column reactors and their influence on chemical engineering processes.

To study the effects of bubble shape on the transport and mixing characteristics, bubbles were simulated for different values of the physical parameters, which were cast in dimensionless numbers, that is, the Morton number $\mathrm{Mo} = g\mu_l^4/(\rho_l\sigma^3)$ and the Eötvös number $\mathrm{Eo} = g\rho_l d_b^2/\sigma$. From the computational results, the bubble Reynolds number $\mathrm{Re}_b = d_b U_t \rho_l/\mu_l$ and the Weber number $\mathrm{We} = d_b U_t^2 \rho_l/\sigma$ $(=\mathrm{Re}_b^2\sqrt{\mathrm{Mo}/\mathrm{Eo}})$ were estimated. For different values of these numbers, bubbles can have various shapes, among which spherical, ellipsoidal, and spherical/elliptical cap are the most frequently encountered.

The front-tracking method[48] accounts for the differences in material properties between the two phases, as well as for interphase momentum exchange occurring at the phase boundary. Because the material properties and the flow fields are discontinuous across the interface, the conservation equations are written in terms of generalized functions. Each fluid is identified by a Heaviside step-function H, which takes a value of one, if fluid 1 is present, and a value of zero anywhere else. The interface between the two phases is marked by δ-functions, thus making it convenient to express H in terms of δ-functions, that is

$$H(x, y, t) = \int_{A(t)} \delta(x - x')\delta(y - y')da' \tag{1}$$

The value of H is 1 if $(x, y) \in A(t)$ and 0, otherwise. In this representation, the interface is identified by a nonzero value of the gradient of H

$$\nabla H = \nabla \int_A \delta(x - x')\delta(y - y')da' \tag{2}$$

The integration is performed in the primed variables and the gradient is taken with respect to the unprimed variables. Therefore, the gradient sign can be placed inside the integral. Performing the differentiation with respect to the primed variables instead of the unprimed variables will result only in reversal of direction

$$\nabla H = \int_A \nabla[\delta(x - x')\delta(y - y')]da' = -\int_A \nabla'[\delta(x - x')\delta(y - y')]da' \tag{3}$$

Using the Gauss–Ostrogradski theorem, the integral over the surface A in Eq. 3 can be transformed into a contour integral over the boundary of A, which will be denoted by S

$$\nabla H = -\oint_S \delta(x - x')\delta(y - y')\mathbf{n}'ds' \tag{4}$$

Equation 4 shows that the costly integration over the entire domain can be substituted with integration over the front for the computation of the gradient of the Heaviside function. The step-function representation allows each variable to be defined for the entire computational domain. Thus, by assuming constant density in each phase

$$\rho(x, y, t) = \rho_1 H(x, y, t) + \rho_0[1 - H(x, y, t)] \tag{5}$$

The fluid viscosity can be represented in the same way. The density gradient is given by

$$\nabla\rho = \rho_1\nabla H - \rho_0\nabla H = (\rho_1 - \rho_0)\nabla H = (\rho_0 - \rho_1)\oint \delta(x - x')\delta(y - y')\mathbf{n}'ds' \tag{6}$$

The Navier–Stokes equations, describing the fluid flow, can then be written as

$$\frac{\partial\rho\mathbf{u}}{\partial t} + \nabla\cdot\rho\mathbf{u}\mathbf{u} = -\nabla P + \rho\mathbf{f} + \nabla\cdot\mu(\nabla\mathbf{u} + \nabla^T\mathbf{u}) + \oint \sigma\kappa'\mathbf{n}'\delta^2(\mathbf{x} - \mathbf{x}')ds' \tag{7}$$

This equation is satisfied for the entire computational domain, regardless of discontinuities in material properties. In Eq. 7, $\mathbf{f}$ is a body force, σ is the surface tension, κ is the curvature of the interface, and δ^2 is a two-dimensional delta-function, equal to the product of $\delta(x - x')$ and $\delta(y - y')$. Assuming incompressible fluids, the continuity equation takes the following form

$$\nabla\cdot\mathbf{u} = 0 \tag{8}$$

The mass-balance equation for a reactive species c_i, with $i = \{A, B, R, S\}$ can be written as

$$\frac{\partial c_i}{\partial t} = -\mathbf{u}\cdot\nabla c_i + D_i\nabla c_i + \sum_j \nu_{i,j} r_j \tag{9}$$

where the summation occurs over the different reactions. $\nu_{i,j}$ represents the corresponding stoichiometric coefficients; A denotes the liquid-phase reactant (such as an unsaturated hydrocarbon); B is a dissolving reactive gas (such as hydrogen); and R and S are product and by-product, respectively. Here

$$c_i(x, y, t) = c_{l,i}H(x, y, t) + c_{g,i}[1 - H(x, y, t)] \tag{10}$$

where $c_{l,i}$ is the concentration of species i in the liquid phase and $c_{g,i}$ is its concentration in the gas phase; $c_{g,B}$, that is, the concentration of the reactive gas B in the bubble, is uniformly constant and is equal to P/H_c; $c_{g,i}$ is zero for all other species.

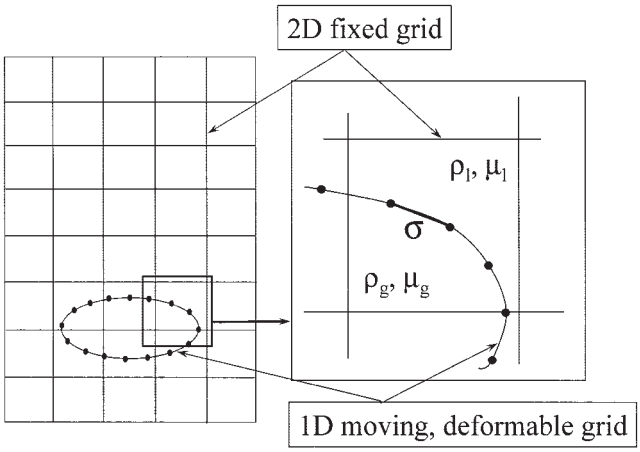

Figure 1. A 2D fixed uniform grid is used to solve the conservation equations, whereas a deformable, moving 1D grid is used to track the interface.

The physical characteristics of the fluid experience a jump at the interface.

This is a reasonable assumption for the cases, where the characteristic residence time of the bubble is short compared to the mass-transfer timescale.

Numerical Solution

The model equations described in the previous section can be solved using methods developed for the simulation of single-phase flows with two additional steps: advection of the phase boundary and computation of the surface tension. In this work the equations are discretized using central finite differences on a fixed, rectangular, staggered grid. A one-dimensional, moving grid is then used to track the interface. The computational grids are shown on Figure 1. Both phases are treated as the same fluid with the physical properties, such as density and viscosity, undergoing a jump at the interface.

Method implementation

The method is carried out in the following steps (see also Tryggvason et al.[48]).

Initial Setup. The initial position of the phase boundary is determined, and the density, viscosity, and concentration fields are computed accordingly. The phase boundary is represented by a moving front, consisting of marker points and the respective connecting elements. Both front points and elements are stored in unordered linked lists. The entry for each member of such a list contains pointers to its two neighboring members. Front representation using linked lists is particularly useful when element removal and addition are considered. The following data are stored for each front point and element: marker point entries contain only the coordinates of the point, whereas element entries contain information about the element end points, other elements connected to the same end points, surface tension, and jumps in material properties at the element.

Integration of the Navier–Stokes Equations. Once the fluid density field is determined for a given interface position, the velocity field can be computed using the following two-step procedure. In the prediction step, the pressure terms are ignored

$$\frac{\rho^{n+1}\mathbf{u}^* - \rho^n\mathbf{u}^n}{\Delta t} = \nabla_h \cdot \rho^n\mathbf{u}^n\mathbf{u}^n + \nabla_h \cdot \mu^n(\nabla_h\mathbf{u}^n + \nabla_h^T\mathbf{u}^n) + \mathbf{F}_\sigma \tag{11}$$

In the correction step, the pressure gradient is added, that is

$$\frac{\rho^{n+1}\mathbf{u}^{n+1} - \rho^{n+1}\mathbf{u}^*}{\Delta t} = -\nabla_h \cdot P \tag{12}$$

Here $n + 1$ represents the new time and n the old time step, whereas * represents the output of the predictor step. The time step is Δt. $\mathbf{F}_\sigma$ denotes the body forces and the surface tension, and the subscript h denotes numerical approximation of the spatial differentiation. The equation ensuring that the velocity at the new time step has zero divergence, that is

$$\nabla_h \cdot \mathbf{u}^{n+1} = 0 \tag{13}$$

can be used to eliminate $\mathbf{u}^{n+1}$ from Eq. 12, leading to

$$\nabla_h \frac{1}{\rho^{n+1}} \nabla_h P = \frac{1}{\Delta t} \nabla_h \cdot \mathbf{u}^* \tag{14}$$

Because the density is variable (depends on the spatial coordinates) this equation cannot be solved using fast Poisson solvers, designed for separable elliptic equations. Instead, an iterative technique, based on the successive over relaxation (SOR) method, is used. The convergence of the solution of the pressure equation depends on the ratio of the gas and liquid densities. For large ratios, small errors can lead to negative densities and cause convergence difficulties. However, the influence of the density ratio on the behavior of the system is relatively small, as the hydrodynamics are determined by the density difference and not the ratio. Therefore, it possible to use smaller density ratios without significantly altering the simulation results. More details on the methods for the solution of the pressure equation and the associated numerical difficulties can be found in Tryggvason et al.[48]

Advecting and Restructuring the Front. Once the fluid velocities are computed, the points that constitute the front are advected to a new position in the domain. Because the velocities are computed on the fixed grid, it is necessary to interpolate the value of the velocity at the interface point, using the fixed grid values

$$\mathbf{u}_f = \sum_{i,j} \omega_{ij}\mathbf{u}_{ij} \tag{15}$$

Here, the summation is over the fixed grid points that are close to the interface point; ω_{ij} are weighing functions and $\mathbf{u}$ is the velocity ($\mathbf{u}_f$ is the value of the velocity of the front and $\mathbf{u}_{i,j}$ is the velocity in the i,jth cell). Once the front point velocities have been determined, explicit Euler integration is used to solve for the new position, according to

$$\mathbf{x}_f^{n+1} = \mathbf{x}_f^n + \mathbf{u}_f^n \Delta t \tag{16}$$

During its motion, the front can stretch and deform. As a result, in some parts of the front, there will be too few points to ensure proper resolution and in other parts, the marker points might become unnecessarily close. Redistribution of the front points is achieved by adding and deleting points when necessary. In two dimensions, the procedure is straightforward. A large element is split by inserting a new point and a small element is deleted by removing a point and connecting its neighbors. When new points are added, the curvature of the front is taken into account by using a higher-order Legendre interpolation. To determine whether a point addition or removal is necessary, minimum and maximum element lengths are defined. If an element is longer than the maximum allowed length, it is split in two and, conversely, if an element is shorter than the minimum length, it is deleted. The limits are selected such as to yield a front resolution comparable to that of the fixed grid.

Updating the Material Properties. Material properties (such as diffusion constant, density, and viscosity) are not advected directly. Instead, they are determined using the position of the phase boundary at each step. The interface marks a jump in material properties, which translates into a steep gradient on the fixed grid. The gradient is given by

$$\nabla \rho = \int \Delta \rho \mathbf{n} \delta(\mathbf{x} - \mathbf{x}_f) ds \tag{17}$$

or

$$\nabla_h \rho_{ij} = \sum_k \Delta \rho \omega_{ij}^k \mathbf{n}_k \Delta l_k \tag{18}$$

In Eq. 18, $\rho_{i,j}$ is the value of the density in the i,jth grid cell, k denotes each front element, and Δs_l is the element length. Once the grid-gradient field has been constructed, the density is computed using the following procedure: Taking the numerical divergence of the grid density gradient results in an approximation of the Laplacian

$$\nabla^2 \rho = \nabla_h \cdot \nabla_h \rho_{ij} \tag{19}$$

After the left-hand side is approximated using centered differences, the solution of the resulting Poisson equation with the appropriate boundary conditions yields the density field everywhere.

Computing the Surface Tension. For the computation of the surface tension the force, acting on a front element, has to be determined

$$\delta \mathbf{F}_\sigma = \int_{\Delta s} \sigma \kappa \mathbf{n} ds \tag{20}$$

Using the definition of the curvature of a two-dimensional line at a point

$$\kappa \mathbf{n} = \frac{\partial \mathbf{s}}{\partial s} \tag{21}$$

the expression for the force can be written as

$$\delta \mathbf{F}_\sigma = \sigma \int_{\Delta s} \frac{\partial \mathbf{s}}{\partial s} ds = \sigma(\mathbf{s}_2 - \mathbf{s}_1) \tag{22}$$

Above, κ is the value of the curvature, $\mathbf{n}$ is the vector normal to the curve at the point, $\mathbf{s}$ is the vector tangential to the line at the point, and s is the arc length parameter. Thus, knowledge of the tangents at the end points of the elements is sufficient, and it is not necessary to compute the element curvature. This approach has two main advantages: it substantially simplifies the computations and it ensures that the total force on any closed surface is zero. Such a conservative property, guaranteed by the fact that the force at the end of each element is exactly equal to the force at the beginning of the next, is useful because it eliminates the possibility of accumulation of small errors over long computations. The tangent to a curve is given by

$$\mathbf{s} = \frac{\partial \mathbf{g}}{\partial s} \Big/ \left\| \frac{\partial \mathbf{g}}{\partial s} \right\| \tag{23}$$

where $\mathbf{g}$, a natural representation of the curve, is numerically approximated by a Legendre polynomial fit through the end points of each element and their neighboring points. This fit will yield different results for two elements sharing a common end point. To avoid this inconsistency the tangents are averaged for each element.

Smoothing of the Values of Front Quantities onto the Fixed Grid. The surface tension is computed on the moving grid tracking the front and is used for the solution of the Navier–Stokes equations on the fixed grid. Therefore, it is necessary to develop a procedure to convert the value of a quantity that exists on the front into a grid value. This procedure is, in essence, an approximation of the δ-function representing the front. To ensure that the transferred quantity is conserved, during this "smoothing," the following relation must be satisfied:

$$\int_{\Delta l} \phi_f(s) dl = \int_{\Delta s} \phi_g(\mathbf{x}) ds \tag{24}$$

Here, ϕ_f is the front quantity, which is expressed in units per length (of the interface), and ϕ_g is the grid value, given in units per area. For a discrete system, Eq. 24 becomes

$$\phi_{ij} = \sum_k \phi_k \omega_{ij}^k \frac{\Delta l_k}{h^2} \tag{25}$$

where ϕ_k is a discrete approximation of the front value ϕ_f; ϕ_{ij} is the grid value; Δl_k is the length of element k; and ω_{ij}^k is the weight of grid point (i, j) with respect to element k. The sum is

over all elements in the front, and h is the grid spacing. The weights must obey

$$\sum_{i,j} \omega_{ij}^{k} = 1 \tag{26}$$

The weights are written as products of one-dimensional functions. The weight for the grid point (i, j) for smoothing from $\mathbf{x}_p = (x_p, y_p)$ is given by

$$\omega_{ij}(\mathbf{x}_p) = d(x_p - ih)d(y_p - jh) \tag{27}$$

The functions d are constructed[65] as

$$\begin{aligned} d(r) &= \left(\frac{1}{4h}\right)\left[1 + \cos\left(\frac{\pi r}{2h}\right)\right] \qquad |r < 2h| \\ &= 0 \qquad\qquad\qquad\qquad\quad |r \geq 3h| \end{aligned} \tag{28}$$

The smoothing procedure is applied to obtain a grid value of the surface tension, as well as to transfer the density gradient from the front onto the grid.

Mass Transport and Chemical Reactions. To achieve the desired accuracy, the chemical species conservation equations are solved on a fixed grid, much finer than the one used for the solution of the Navier–Stokes equations. Because gas depletion inside the bubble is not considered, at each time step the interface is resolved onto the fine fixed grid, and the concentration of the gas-phase reactant gas is set equal to the equilibrium concentration $c_{b,eq} = P/H_c$. P is the reactive-gas partial pressure inside the bubble and H_c is the Henry constant for the gas–liquid system. For the computation of the species advection, the fluid velocities need to be interpolated from the coarse grid onto the fine grid. Because both grids are staggered, direct interpolation of the velocities would yield fine-grid values, which will not satisfy the continuity equation. To circumvent this problem, the following procedure was developed (Figure 2).

For each fine-grid cell:

(1) The four nearest coarse-grid cell faces and cell centers surrounding the fine-grid cell are identified.

(2) The coarse-grid cell face velocity values are used to interpolate the velocities on two of the faces of the fine-grid cell (such as south and east) (Figures 2a and 2b).

(3) The spatial derivatives of the velocity components are computed at the four coarse-grid cell centers. These are then used to interpolate the value of the derivatives at the center of the fine-grid cell (Figure 2c).

(4) The interpolated derivatives are then used, together with the interpolated velocities at two of the faces, to obtain the velocities at the remaining two cell faces (Figure 2d). Thus if $u_{i-1,j}$ (the horizontal component of the velocity at the western face) was interpolated, u_i will be given by

$$u_{i,j} = \left(\frac{\partial u}{\partial x}\right)_{ij}^{\text{int}} \Delta x + u_{i-1,j}^{\text{int}} \tag{29}$$

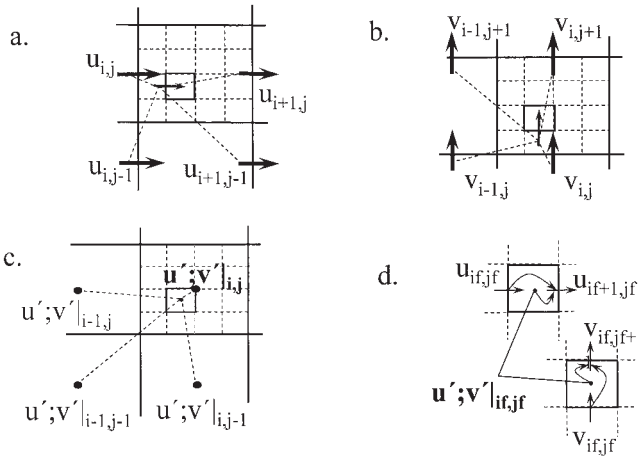

Figure 2. Interpolation of the velocities from the coarse onto the fine grid.

(a) Interpolation of the velocity at the east face of the fine cell from the coarse values; (b) interpolation of the velocity at the south face of the fine cell from the coarse values; (c) interpolation of the velocity derivatives in the center of the fine cell from the coarse values; (d) computation of the west and south face velocities.

Here the superscript "int " designates an interpolated value. This formulation guarantees continuity. For all interpolations, a second-order bicubic scheme was used.[66]

Once the fine-grid velocities are obtained, the new concentration field is computed according to

$$c_i^n = c_i^{n-1} - \Delta t\left(\mathbf{u}\cdot\nabla c_i^{n-1} - D_i\nabla^2 c_i^{n-1} - \sum_j \nu_{ij} r_j\right) \tag{30}$$

The model equations are advanced in time using a second-order Adams–Bashford integration scheme.

Although not necessary, in our model the depletion of the gas inside the bubble is neglected. Thus, by assuming that the bubble only contains a single species and by neglecting pressure gradients inside the bubble, the concentration of the dissolved gas within the area enclosed by the interface must stay constant. To achieve this, at each time step the density is computed on the fine grid using the procedure outlined in step 3 for the current location of the front. As a result, a density field is obtained on the fine grid, with the density equal to the density of the gas inside the bubble and to that of the liquid, outside.

The concentration of the gas is then set equal to $c_{g,B} = P/H_c$ everywhere in the domain, where the density is equal to ρ_g. The mass transfer across the interface is therefore computed with a resolution equal to the length of a fine grid cell, that is, 1/600th of the width, which gave grid independence.

Computation parameters

The computational domain used in our simulations has a rectangular shape and dimensions of $12d_b \times 36d_b$. Several different grid resolutions were considered for the hydrodynamic computations. The two main factors affecting the choice of resolution are conservation of the area enclosed by the

Table 1. Values of the Dimensionless Numbers Describing the System

Re_b	8–68
Sc_i	62–431
Pe	3448–4216
We	1.3–3.0
Mo	5×10^{-7}–1.2×10^{-3}
Eo	3.125–8.0

interface and computational time. During the advection and restructuring of the front, the enclosed area can fluctuate. The size of these fluctuations decreases at higher grid resolution. The resolution used (200×600 cells) results in area fluctuations of $<1\%$ (for a bubble rising with $Re_b = 68$, over 100,000 time steps) and a computational time of 15 to 25 days, depending on the system. The corresponding grid resolution used for the mass transport and reaction computations was 600×1800 cells, which was needed to resolve the interface transport and the mixing in the liquid phase. This number also illustrates why a 3D DNS of reacting bubbles is currently infeasible because $O(10^9)$ grid points would be required. Computations were carried out on a six-processor Linux cluster (2-GHz Pentium with 2GB of RAM each).

Periodic boundary conditions were implemented at the top, bottom, and both walls of the domain, ensuring that a fluid particle exiting the domain from one side will reenter it from the other with the same velocity. The same boundary conditions were used for the species transport computations, as well.

The time step used in the computations was computed as

$$\Delta t = 0.1 \frac{(\Delta x)^2}{4\beta} \tag{31}$$

where β is the larger one of the gas- and liquid-phase viscosity-to-density ratios, that is $\beta = \max(\mu_l/\rho_l, \mu_g/\rho_g)$. Because large density ratios can lead to problems in the solution of the Navier–Stokes equations, a relatively small ratio of 1:10 was used. Since most interactions depend on the difference in density and not the ratio,[48] as long as the value of the density jump across the interface is kept realistic, the ratio used does not cause a significant deviation in the results.

In Table 1, the parameters for our simulations are given, which are typical for many industrially important gas–liquid reactions. The characteristic length, on which the dimensionless numbers are based, is the equivalent spherical diameter of the bubble, and the characteristic velocity, the terminal rise velocity of the bubble.

Validation

Validation of the hydrodynamic model was achieved through a comparison of the results to known analytical and CFD solutions as well as experimental data, which is discussed in detail by Tryggvason et al.[48] and Sankaranarayanan et al.[49] For the validation of the mass-transfer/liquid-phase transport model, a comparison was carried out between simulation results and experimental data found in the literature and is presented in later sections.

Results

Hydrodynamics

The set of equations described in the preceding sections was used to simulate the buoyancy-driven rise of bubbles in an initially quiescent liquid for different sets of system properties (see Table 1). Figure 3 shows snapshots of the flow fields resulting from a single rising bubble at three different Reynolds number in a stationary reference frame. Stream traces are shown instead of the actual vector plots because of the high numbers of grid cells (600×1800). Figure 3a shows the flow field associated with a single bubble rising at terminal velocity with $Re_b = 8$. The shape of the bubble is approximately elliptical, and it rises in a straight vertical path. This motion causes two symmetric recirculation cells to form on each side of the bubble, with liquid in the wake directly behind the bubble flowing up and then falling down on the sides. With the exception of the slightly increased size of the recirculation cells, the flow field for $Re_b = 12.5$ (not shown) is identical.

At higher Reynolds numbers, above some critical value, the vortex-shedding regime develops, in which vortices form periodically on alternating sides behind the bubble. These vortices grow and after having achieved a certain size they detach and drift away from the bubble, forming a von Kármán vortex street in the bubble wake. Because of the vortex-shedding process, the lift force oscillates periodically between a positive and a negative value,[3] causing the bubble to move in a zigzag-like trajectory. Figures 3c and 3d show two snapshots of a bubble rising in the vortex-shedding regime at $Re_b = 68$.

Figure 4 shows the flow fields for Re_b values of 8, 12.5, and 68 in a coordinate system moving with the bubble (that is, a system, in which the bubble is motionless). The transition to this system is achieved through transformations, accounting for bubble translation, rotation, and deformation. From this plot, it can be seen that there are fundamental differences between the three flow fields. In the case of $Re_b = 8$, the liquid flows around the bubble with stream traces closing at the bottom. In the case of $Re_b = 12.5$, a recirculation zone, consisting of two symmetric counterrotating cells, forms in the wake of the bubble, as described in Koynov and Khinast.[3] Inside the bubble, two sets of counterrotating cells form. This difference is undetectable in the fixed coordinate system. As the Reynolds number increases

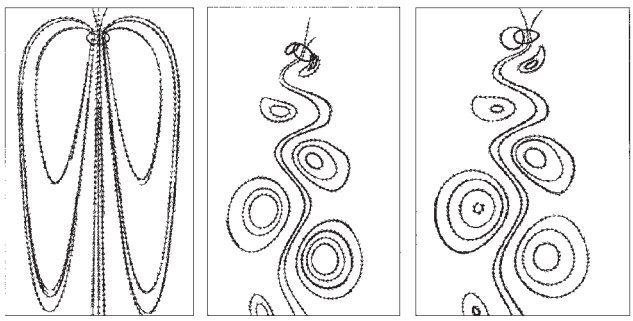

Figure 3. Stream trace plots of the flow fields associated with the motion of single deformable bubbles.

(a) $Re_b = 8$, Eo = 3.125, Mo = 1.2×10^{-3}; (b, c) $Re_b = 68$, Eo = 3.125, Mo = 1.2×10^{-3}.

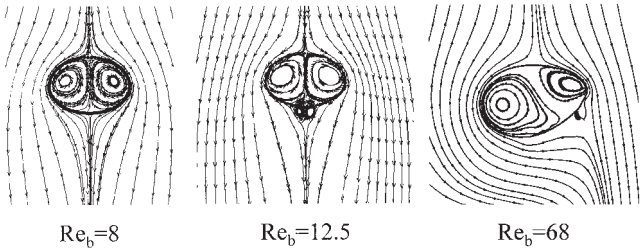

Figure 4. Stream trace plots of the flow fields associated with the motion of single deformable bubbles in a reference frame attached to the bubble.

(a) $Re_b = 8$, Eo = 3.125, Mo = 1.2×10^{-3}; (b) $Re_b = 12.5$, Eo = 3.125, Mo = 3.1×10^{-4}; (c) $Re_b = 68$, Eo = 3.125, Mo = 1.2×10^{-3}.

(such as that caused by a decrease of the liquid viscosity), the size of the recirculation zone in the wake increases as well. However, because of its symmetry, the net lift force acting on the bubble remains zero and its motion does not deviate from the vertical path. Above a certain Reynolds number, in the vortex-shedding regime, the bubble rises in a nonlinear path, with its shape deforming considerably. Figure 4c shows the flow fields inside and in the wake of such a deformed bubble. The vortex-shedding process leads to a break of symmetry in the wake, which leads to the destruction of the symmetry of the circulation cells inside the bubble.

In our simulations, the transition to the vortex-shedding regime occurs at Reynolds numbers between 30 and 50. Vortex shedding is caused by the generation of sufficient vorticity at the bubble surface, which cannot be removed by diffusion. Given that vorticity is generated at rates inversely proportional to the curvature of the interface, the onset of vortex shedding will depend on the bubble shape. An increase in the Reynolds number can be achieved either by decreasing the viscous forces (equivalent to decreasing the Morton number for σ = const.) or by increasing the inertial forces (equivalent to increasing the Weber number for σ = const.). This is illustrated in Figure 5. As the Morton number decreases, the shape of the bubble changes from nearly circular to elliptical (the aspect ratio $\delta = d_{max}/d_{min}$ of the ellipse decreases with the Morton number). In the case of an increase of the Weber numbers, the bubble shape changes from nearly circular to elliptical, to elliptical cap (Figure 5). Therefore, the transition to the vortex-shedding

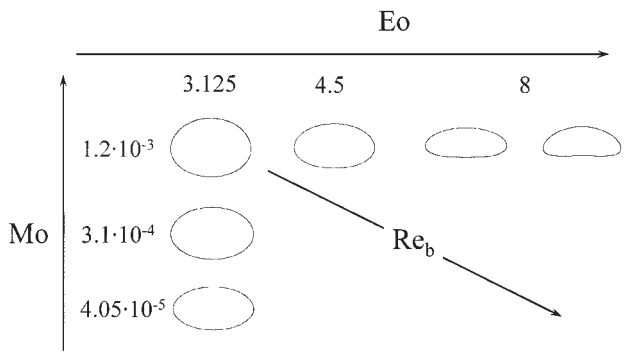

Figure 5. Variations of bubble shapes with changes in the Eötvös and Morton numbers.

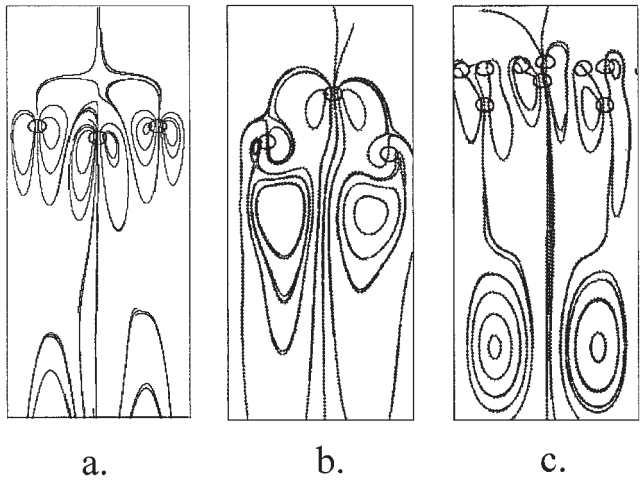

Figure 6. Stream trace plots of the flow fields associated with the motion of bubble swarms.

(a) Case 1; (b) case 2; (c) case 3.

regime depends not only on the Reynolds number itself, but also on the set of Morton and Weber numbers, which lead to a specific Re_b.

To study the hydrodynamics of bubble clusters, three different cases of multiple bubbles rising simultaneously were chosen for the same conditions that led to a single bubble with $Re_b = 8$ in Figure 3. The cases differ by the number of bubbles and by their initial positions. In case 1, three identical, initially circular bubbles (Eo = 3.125, Mo = 3.1×10^{-4}) were positioned in a horizontal line, with the distance between every two neighboring bubble centers being equal to six times the bubble radius. Case 2 differs from case 1 only in the starting position of the bubbles. In this case, the bubbles were arranged in a vertical line. The inter-bubble distances were kept the same. In case 3, nine bubbles, identical to the ones considered in cases 1 and 2 were arranged in a square pattern with three bubbles on each side. The distance between every two vertical or horizontal neighbors was kept equal to six bubble radii. Figure 6 shows several stream-trace plots of the flow fields associated with the flow developing in each case.

In case 1 (Figure 6a), as the bubbles rise, the distance between them increases to some stable value. Once this distance is established, the three bubbles rise together, keeping the horizontal equidistant formation. Near the bubbles, the wake consists of the three typical wakes of the bubbles rising side by side. Far from the bubbles a secondary wake can be seen, which resembles the wake of a bubble with a size roughly equal to the size of the entire bubble cluster. It is interesting to note that in this configuration (that is, a periodic box, which leads to downflow between the bubbles) the three bubbles slow each other down, resulting in a Reynolds number of around 6.5 (compared to the Reynolds number of a single bubble, which is equal to 8). In case 2 (Figure 6b), the initial vertical configuration is quickly destroyed and the motion of each bubble can be seen as a combination of two separate motions: the general upward motion, which is now faster than that in the case of a single bubble ($Re_b = 9.5$), and a secondary motion of each bubble with respect to the other two. The second type of motion is very complex and depends strongly on bubble–

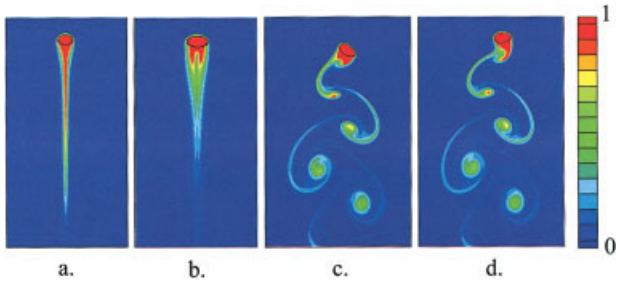

Figure 7. Contour plots of the dimensionless concentration fields of the dissolved gas around a single deformable bubble.

(a) $Re_b = 8$, Eo = 3.125, Mo = 1.2×10^{-3}, Sc = 430; (b) $Re_b = 12.5$, Eo = 3.125, Mo = 3.1×10^{-4}, Sc = 300; (c, d) $Re_b = 68$, Eo = 3.125, Mo = 5×10^{-7}, Sc = 60. [Color figure can be viewed in the online issue, which is available at www.interscience.wiley.com.]

bubble interactions. The wakes of the individual bubbles are suppressed and the entire cluster leaves a wake as if it were an integral structure. After sufficient time has passed, the three bubbles of cases 1 and 2 behave in an identical way. Figure 6c shows case 3, that is, nine bubbles. The Reynolds number that is reached is approximately 8. Based on these results, it becomes apparent that the flow fields in swarms can vary drastically from those around individual bubbles and that modeling of individual bubbles is insufficient to understand the dynamics of realistic multiphase flows.

As the flow fields within the swarm develop as a result of both the wake dynamics of individual bubbles and bubble–bubble interactions, the behavior of the swarm as a whole will depend both on the properties of its constituent bubbles and on their interactions. The significance of this observation is that averaged motion models, used for the design of industrial equipment, need to take into account the behavior characteristic of swarms, which cannot be replicated with single bubbles.

Mass transfer

As the parameters of the multiphase system (Weber number, Morton number, Schmidt number, and number of bubbles) change, so does the rate of gas–liquid interfacial mass transfer. The reason for these changes is twofold. As the bubble shape changes (as a function of We and Mo), the bubble volume-to-interfacial surface area ratio will change as well. Furthermore, the hydrodynamics can strongly affect the mass-transfer rate by the concentration boundary layers and the transport of the dissolved gas near the bubble surface. These two factors cannot be treated separately because they are intrinsically connected.

Several simulations were performed of bubble motion with mass transfer under different conditions. Figure 7 shows the dimensionless concentration profiles of the dissolved gas around different single bubbles for an unreactive system. The concentration has been made dimensionless using the equilibrium concentration $c_{b,eq} = P/H_c$. The plot in Figure 7a corresponds to $Re_b = 8$. In this case, as can be seen from Figures 3a and 3b, the bubble wake is closed and the liquid flows smoothly around the bubble. The dissolved gas is contained exclusively in the bubble wake. The plot in Figure 7b ($Re_b = 12.5$) resembles the one in Figure 7a with one notable exception. Dissolved gas becomes trapped in the twin recirculation cells in the bubble wake (seen in Figure 3b), resulting in two high-concentration regions. It has been shown[3] that the residence time of chemical species trapped in these regions can be large, compared to other portions of the wake, which can lead to changes in selectivity for certain mixing-sensitive reactions. Figures 7c and 7d show two different snapshots of the dissolved gas concentration for the case of $Re_b = 68$ (vortex-shedding regime). Vortices form alternately on each side of the bubble, grow, and drift away, transporting entrapped dissolved gas down the wake, that is, patches rich in the dissolved gas are formed and are convected away from the bubble, leading to fast dispersion of the gas in the liquid. From these figures, it is evident that the residence time in a recirculatory wake is larger than the one for vortex shedding. If the residence times of the reactants in the wake are important, the selectivity of the two regimes may be quite different. Reactive-flow computations discussed below will illustrate this point.

It is apparent from the plots in Figure 7 that the changes in hydrodynamics, following an increase in the Reynolds number, can have a significant impact on the gas–liquid mass transfer. This effect is illustrated in Figure 8, which shows the Sherwood number divided by the square root of the Peclet number ($Sh/\sqrt{Pe} = k_L\sqrt{d_b/U_tD_L}$) as a function of the Reynolds number. Here the overall k_L has been computed by the rate of increase of the total amount of dissolved gas in the domain, normalized by the length of the gas–liquid interface. It can be seen that the rate of mass transfer increases, steeply at first, and then more moderately, above a certain Reynolds number. Figure 8 also includes two sets of data points experimentally determined by Redfield and Houghton,[67] as well as the modified Boussinesq equation for an inviscid spherical bubble $Sh/\sqrt{Pe} = 1.13 \times (1 - 2.96/\sqrt{Re_b})^{0.5}$.[68] The match between our results and experimental data is very good, given that the same Reynolds number can be obtained by various sets of system parameters, leading to different bubble shapes. At lower Reynolds numbers, the values generated by our simulations are somewhat higher than those suggested by the Boussinesq equation. This can be explained by the fact that the Boussinesq equation is usually used for higher Reynolds.

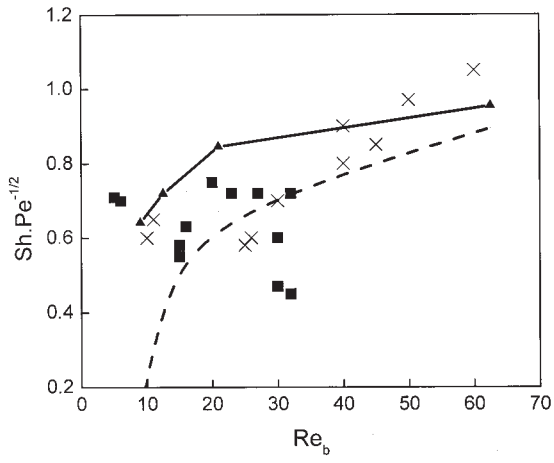

Figure 8. Mass-transfer rates as a function of the Reynolds number.

▲: Our simulations; ■ and ×: data from Redfield and Houghton[67]; dashed line: modified Boussinesq equation.

In bubble swarms, bubbles no longer travel by themselves, but rather in liquid perturbed by the wakes of neighboring bubbles. This leads to liquid-phase flow fields, which will differ significantly from those around single bubbles. Another consequence of a bubble moving in a swarm is that the concentration of gas dissolved in the liquid around the bubble will no longer depend only on the mass transfer from the bubble itself, but also on the mass transfer from the other bubbles in the swarm. These two factors can have a significant impact on the mass-transfer rate. To study the gas–liquid mass transfer in bubble swarms, the mass-transfer rates were computed for the three cases described earlier (a group of three bubbles initially positioned in a horizontal line and a vertical line, and nine bubbles arranged in a square pattern). Figure 9 shows snapshots of the dimensionless concentration fields of the dissolved gas for the three cases. It can be seen that, as the motion of each bubble in the first case strongly resembles that of a single bubble, the concentration fields around each bubble also match these around a single bubble. However, for nine bubbles, groups of three bubbles develop, which act as one *superbubble*. Figure 10 shows the values of the Reynolds number and of $\mathrm{Sh}/\sqrt{\mathrm{Pe}} = k_L\sqrt{d_b/U_t D_L}$ for each cluster case, as well as the corresponding values for a single bubble. The values shown are per bubble (not per cluster). It can be immediately seen that the mass-transfer coefficient of the swarms is lower, independent of the Reynolds number. The mass-transfer rate in case 1 is lower than that for a single bubble because of the lower Reynolds number. In fact, the value lies very close to the single-bubble curve in the (Re_b, $\mathrm{Sh}/\mathrm{Pe}^{-1/2}$) plane. In the second case, the mass-transfer rate is again lower than that for a single bubble. This can be explained by the fact that, as the three bubbles move with respect to each other, one bubble will often travel in the wake of another. This will lead to a decreased dissolved-gas gradient around the bubble and, consequently, lower mass transfer. In case 3, the situation is analogous.

Liquid-phase chemical reactions

It has been shown, so far, that the liquid-phase hydrodynamics and the gas–liquid mass-transfer rates in gas–liquid multiphase flows can vary substantially, depending on the system parameters. It follows that these differences will also influence reaction yields and selectivities in the case of mixing-sensitive reactions. To investigate the effect of the hydrodynamics on

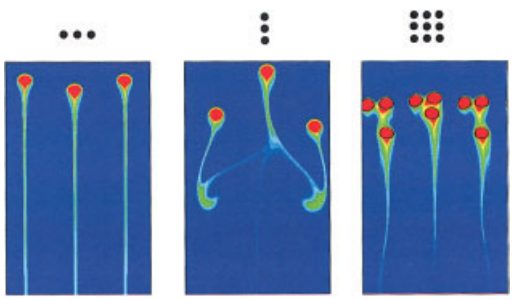

Figure 9. Contour plots of the dimensionless concentration fields of the dissolved gas from bubbles in swarms.

(a) Case 1; (b) case 2; (c) case 3. [Color figure can be viewed in the online issue, which is available at www.interscience.wiley.com.]

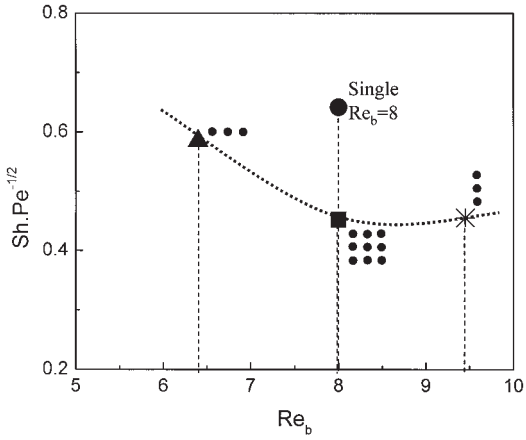

Figure 10. Mass-transfer rates from bubbles in swarms.

▲: case 1; ✳: case 2; ■: case 3; ●: single bubble with $\mathrm{Re}_b = 8$, $\mathrm{Eo} = 3.125$, $\mathrm{Mo} = 1.2 \times 10^{-3}$.

chemical reactions, several simulations were performed for reactive bubbles. In these simulations, gas B is dissolving from the bubble(s) into the liquid phase, where it reacts with reactant A, to form product R. This product R can then react with A to form a by-product S. The reaction network thus is

$$\begin{aligned} A + B &\rightarrow R \\ R + A &\rightarrow S \end{aligned} \tag{32}$$

The reaction rates of these two reactions are

$$r_1 = k_1 c_A c_B \tag{33}$$

and

$$r_2 = k_2 c_R c_A \tag{34}$$

respectively. The Damköhler numbers of the two reactions are defined as

$$\mathrm{Da}_1 = \frac{d_b k_1 c_{A,in}}{U_t} \qquad \mathrm{Da}_2 = \frac{d_b k_2 c_{A,in}}{U_t} \tag{35}$$

The values of the reaction rate coefficients were chosen to result in a Damköhler number for the first reaction (Da_1) equal to 0.25 and a ratio ($\mathrm{Da}_1/\mathrm{Da}_2$) equal to 10. The selectivity toward the product R is computed as

$$Y_R = \frac{\bar{c}_R}{\bar{c}_R + \bar{c}_S} \tag{36}$$

where $\bar{c}_R$ and $\bar{c}_S$ are the volume-averaged dimensionless concentrations of product R and by-product S in the domain.

Figure 11 shows a plot of the selectivity toward R vs. dimensionless time for the two cases of single rising bubbles ($\mathrm{Re}_b = 8$ and $\mathrm{Re}_b = 68$). Clearly, as time progresses the selectivity decreases because the intermediate product will be consumed by reactant A. However, there are noticeable differ-

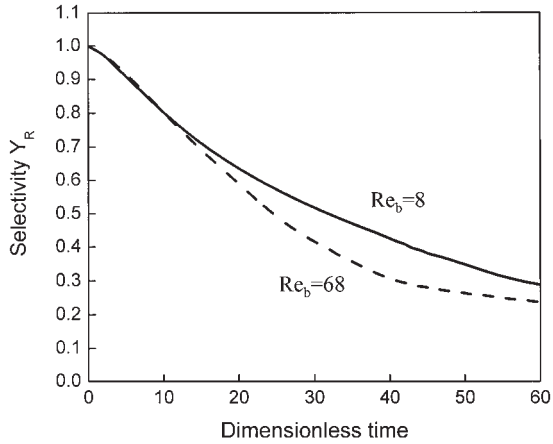

Figure 11. Selectivity toward product R in the case of a single rising bubble.

Solid line: $Re_b = 8$; dashed line: $Re_b = 68$.

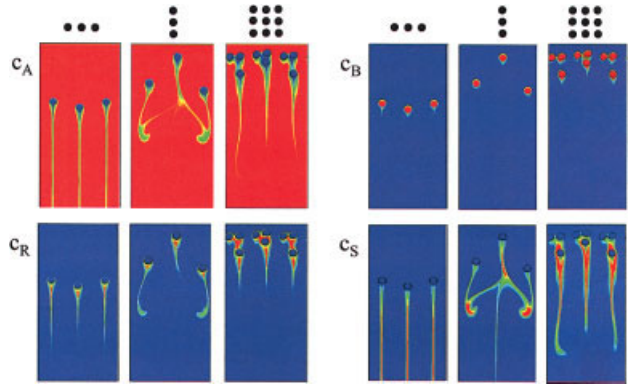

Figure 13. Contour plots of the dimensionless concentration fields of reactant A, reactant B, product R, and by-product S for different bubble swarms.

[Color figure can be viewed in the online issue, which is available at www.interscience.wiley.com.]

ences between the two cases, with the selectivity in the case of the bubble rising in the vortex-shedding regime ($Re_b = 68$) being significantly lower. The difference between the two simulations becomes noticeable only after a certain amount of time ($t = 15$), that is, once the $Re_b = 68$-bubble has developed the vortex-shedding regime (bubbles start from rest). To explain this difference, the instantaneous concentration fields for the two reactants and the two products are shown in Figure 12 for both cases. It can be seen that in the case of $Re_b = 8$, the dissolved gas remains confined in an isolated area in the bubble wake, where it reacts with reactant *A*, forming *R* and depleting *A* to a large extent in the process. Because transport into the wake is relatively slow in this regime,[3] the supply of fresh reactant *A* will be limited, leading in turn to a limited production of *S*. In the case of the bubble rising in the vortex-shedding regime, on the other hand, both the dissolved gas and the product *R* are rapidly dispersed in the wake by the vortex motion. As a result, product *R* is free to react with the available reactant *A* and form the by-product *S*. This process results in a faster decrease of the selectivity toward *R*, which can be observed in Figure 11.

The investigation of chemical reactions was extended to the motion of bubble clusters as well. Again, the three cases described earlier were considered with the chemical reactions (Eq. 32) taking place in the liquid phase. Figure 13 shows several snapshots of the dimensionless concentration fields of the two reactants and the two products for all three cases. Clearly, the combined action of bubbles forming bubble clusters leads to localized high concentrations of *R*. However, the larger structure arising from the cluster also leads to a depletion of *A*, reducing the undesired side reaction. The consequences of the different concentration profiles can be seen on the plot in Figure 14. This plot shows the selectivity toward the product *R* vs. dimensionless time for the three clusters as well as for single bubbles rising in the steady and vortex-shedding regimes. The low Reynolds number and closed wakes in the first swarm case lead to a very high selectivity, similar to the single

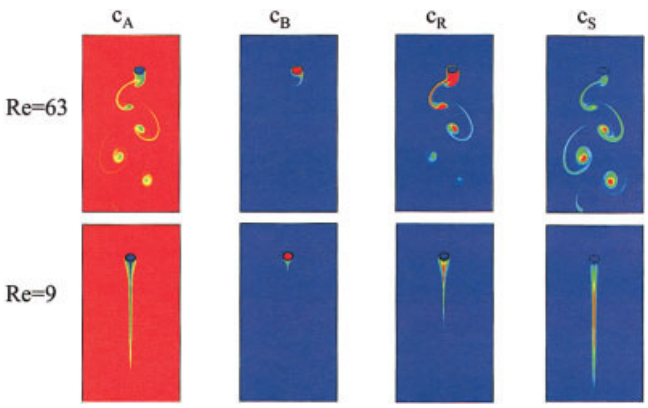

Figure 12. Contour plots of the dimensionless concentration fields of reactant A, reactant B, product R, and by-product S for the case of a single bubble at $Re_b = 8$ and $Re_b = 68$.

[Color figure can be viewed in the online issue, which is available at www.interscience.wiley.com.]

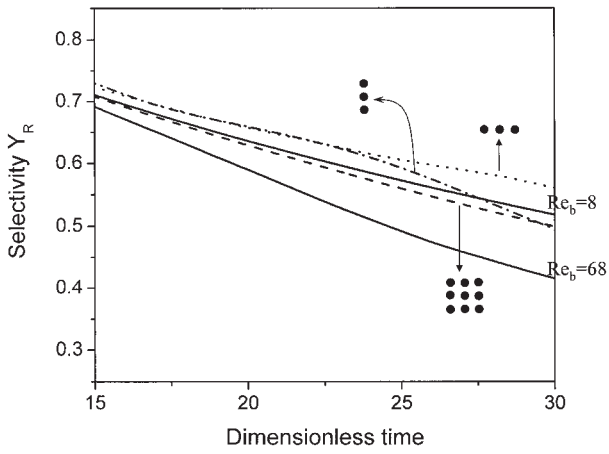

Figure 14. Selectivity toward product R for the three cases of rising bubble swarms.

Dotted line: case 1; dot-and-dash line: case 2; dashed line: case 3. The two solid lines: single bubble for $Re_b = 8$ and $Re_b = 68$.

bubble case. In the beginning, the bubbles in case 2 travel in a line behind each other. This motion leads to a steady wake and a high selectivity. As the structure breaks and the bubbles start moving with respect to each other, the mixing in the liquid phase is improved, and reactant *A* is available in larger quantities in the wake, where it can react with the product *R* to produce *S*. This causes a gradual decrease in selectivity. In case 3, the uniform bubble configuration is destroyed very quickly, and *A* is mixed into the wake rather quickly, which reduces the selectivity. However, all three bubble swarms have a higher selectivity than the vortex-shedding case, which provides the best mixing and thus leads to the lowest selectivity.

Summary and Conclusions

Numerical simulations were performed to study the hydrodynamics, mass transfer, liquid-phase mass transport, and chemical reactions in bubble flows with dynamically evolving interfaces. Specific cases included the buoyancy-driven motion of a single bubble under different conditions (different Morton and Eötvös numbers) and of several bubble clusters of different shapes and bubble counts. The main results of these simulations are as follows:

- It was confirmed that the single-bubble hydrodynamics can vary significantly depending on the system parameters. At low Reynolds numbers a bubble rises in a straight, vertical trajectory. The ensuing wake is closed and steady. At higher Reynolds numbers, the wake loses its stability and vortices are shed periodically behind the bubble. The resulting fluctuations in the lift coefficient cause the bubble to change shape periodically and to move in a serpentine (zigzag-like) trajectory.
- It was also demonstrated that the dynamics of a single bubble differ significantly from those of a bubble moving in a swarm (even for identical bubbles). In the case of swarms, the motion of the system has two components: (1) the vertical motion of the cluster as a whole and (2) the interswarm motion of the individual bubbles with respect to each other.
- Our hypothesis was confirmed that both the gas–liquid mass-transfer and chemical reactions may be very sensitive to the system hydrodynamics. The results of our simulations clearly showed that the mass-transfer rates and chemical reaction selectivities can differ considerably in the various flow regimes. In the case of single bubbles, the mass-transfer rate quickly increases with the increasing Reynolds number until the vortex-shedding regime is reached. Beyond that point, the rate increase slows down. Mass transfer in a bubble swarm depends both on the motion of the swarm as a whole and on the motion of the individual bubbles and, in general, does not follow trends observed in the single bubble cases.
- The chemical reaction system considered in our simulations was shown to be mixing sensitive, that is, its selectivity changed as a function of the liquid-phase mixing characteristics. A typical example of this sensitivity is the high selectivity for single bubble flows at low Reynolds numbers, resulting from the formation of stagnated zones in the wake. It was shown that the complex motion of a bubble traveling in a swarm will lead to flow mixing characteristics and, consequently, reaction selectivity different from that observed in the case of the same bubble rising alone.

The most important outcome of this work is that we are able to study bubble swarms and the impact of the swarm hydrodynamics on reactions systems. This is the first study of its kind reported in the literature. Its importance is paramount because knowledge of the unique flow dynamics inside bubble swarms is crucial to understanding the mechanisms controlling mass transport and chemical reactions in many relevant reactive systems.

Future Work

Our group is currently working on performing simulations on larger computer clusters. The resulting increase in achievable grid resolutions will allow:

- *Simulations closer to the churn-turbulent regime*. Most industrial applications are operated in the churn turbulent regime. To carry out realistic simulations of the flow in this regime, bubble breakup and coalescence must be taken into account.
- *3D simulations*. Three-dimensional simulations of bubbly flows will allow the study of rise trajectories and wake geometries, which cannot be observed in 2D. However, reactive flow computations in 3D seem to be out of reach with the current computational resources [that is, $O(10^9)$ equations need to be solved simultaneously].
- *Large swarms*. Simulations of large swarms, that is, 100 and more bubbles will allow us to explore how the complexity of the flow field increases with the size of the swarm.
- *Catalytic slurries*. The simulations of the motion of suspended catalytic particles performed by our group[1] will be extended to the case of bubble swarms, allowing us to identify the optimal particle properties for given processes.

Acknowledgments

J.G.K. gratefully acknowledges support of this work by the National Science Foundation (NSF) CAREER Award (CTS-0093129) and NSF Grant CTS 02098764.

Notation

A = area of space enclosed by the bubble interface
$c_{A,in}$ = initial concentration of reactant A in the liquid, kmol/m^3
c_i = concentration of species i ($i = A, B, R, S$), kmol/m^3
c_i^k = concentration of species i ($i = A, B, R, S$) during time step k, kmol/m^3
$c_{l,i}$ = concentration of species i ($i = A, B, R, S$) in the liquid phase, kmol/m^3
$c_{g,i}$ = concentration of species i ($i = A, B, R, S$) in the gas phase, kmol/m^3
D_i = diffusion coefficient for species i ($i = A, B, R, S$), m^2/s
d = Peskin smoothing function
d_{max} = major axis of an ellipse, m
d_{min} = minor axis of an ellipse, m
Da_j = Damköhler number of the jth reaction, $Da_j = d_b k_j c_{A,in}/U_t$
da' = area element, $dxdy$, m^2
d_b = equivalent circle diameter, m
ds' = differential element of the bubble contour, m
Eo = Eötvös number, Eo = $g\rho_l d_b^2/\sigma$
$\mathbf{f}$ = body forces, N
$\mathbf{F}_\sigma$ = body and surface tension forces, N
g = gravitational acceleration, m/s^2
$\mathbf{g}$ = natural representation of a curve
H = Heaviside function
h = grid spacing, m
H_c = Henry constant, Pa·m^3/kmol
k_j = reaction rate constant of the jth reaction, m^3/kmol/s
k_L = liquid-side mass-transfer coefficient, m/s
Δl_k = length of the kth front element, m
Mo = Morton number, Mo = $g\mu_l^4/(\rho_l\sigma^3)$

$\mathbf{n}$ = vector normal to the bubble interface
$\mathbf{n}_k$ = vector normal to the kth element of the front
P = pressure, Pa
Pe = Peclet number, PE = $U_t d_b/D$
r_j = reaction rate of the jth reaction, kmol/m^3·s
Re_b = bubble Reynolds number, $\mathrm{Re}_b = d_b U_t \rho_l/\mu_l$
S = contour of the bubble
$\mathbf{s}$ = vector tangential to the front
s = arc length parameter
Sc_i = Schmidt number of species i ($i = A, B, R, S$), $\mathrm{Sc}_i = \mu/\rho D_i$)
Sh = Sherwood number, Sh = $k_L d_b/D$
t = time, s
$\mathbf{u}$ = velocity vector, m/s
$\mathbf{u}_f$ = velocity of the front, m/s
$\mathbf{u}_f^k$ = velocity of the front during the kth time step, m/s
$u_{i,j}$ = x-component of the velocity at the eastern face of cell i,j, m/s
$\mathbf{u}_{i,j}$ = velocity in the i,jth cell, m/s
$\mathbf{u}^k$ = velocity at the kth time step, m/s
$\mathbf{u}^*$ = predicted velocity, m/s
U_t = terminal rise velocity, m/s
We = Weber number, We = $d_b U_t^2 \rho_l/\sigma$
$\mathbf{x}$ = position vector
x = x-coordinate
x' = x-coordinate of points lying inside the bubble interface
$\mathbf{x}_f^k$ = position of the front during the kth time step
x_p = location of grid point p
$\mathbf{x}_p$ = x-coordinate of grid point p
Y_R = selectivity toward product R
y = y-coordinate
y' = y-coordinate of points lying inside the bubble interface
y_p = y-coordinate of grid point p

Greek letters

β = largest of the viscosity/density ratios for the two phases
κ = curvature
μ_l = liquid-phase viscosity, Pa·s
μ_g = gas-phase viscosity, Pa·s
$\nu_{i,j}$ = stoichiometric coefficient of species i in reaction j
ρ^k = density at the kth time step, kg/m^3
ρ_l = liquid-phase density, kg/m^3
ρ_g = gas-phase density, kg/m^3
ρ_i = density of ith phase ($i = 0, 1$), kg/m^3
$\rho_{i,j}$ = density in the i,jth cell
σ = surface tension, N/m
ϕ_f = variable on the front
ϕ_g = variable on the grid
ϕ_k = discrete, grid approximation of ϕ_f (value on the kth element)
$\omega_{i,j}$ = weighing functions

Literature Cited

1. Raffensberger J, Koynov A, Glasser B, Khinast J. Influence of particle properties on the yield and selectivity of fast heterogeneously catalyzed gas–liquid reactions. *Int J Chem Reactor Eng.* 2003;1:A-15.
2. Khinast JG. Impact of 2-D bubble dynamics on the selectivity of fast gas–liquid reactions. *AIChE J.* 2001;47:2304-2319.
3. Koynov A, Khinast J. Effects of hydrodynamics and Lagrangian transport on chemically reacting bubble flows. *Chem Eng Sci.* 2004; 59:3907-3927.
4. Ramachandran PA, Chaudhari RV. *Three Phase Catalytic Reactors*. New York, NY: Gordon & Breach; 1983.
5. Mills PL, Chaudhari RV. Reaction engineering of emerging oxidation processes. *Catal Today.* 1999;48:17-29.
6. van Krevelen DW. Micro- and macro-kinetics. *Chem Eng Sci.* 1958; 8:5-17.
7. Kramers H. Physical factors in chemical reaction engineering. *Chem Eng Sci.* 1958;8:45-58.
8. Danckwerts PV. The effect of incomplete mixing on homogeneous reactions. *Chem Eng Sci.* 1958;8:93-102.
9. Paul EL, Treybal RE. Mixing and product distribution for a liquid phase, second order, competitive-consecutive reaction. *AIChE J.* 1971; 17:718-724.
10. Bourne JR, Crivelli E, Rys P. Chemical selectivities disguised by mass diffusion. V. Mixing-disguised azo coupling reactions (Sixth communication on the selectivity of chemical processes). *Helv Chim Acta.* 1977;60:2944-2957.
11. Nienow AW, Drain SM, Boyes AP, Mann R, El-Hamouz AM, Carpenter HJ. A new pair of reactions to characterize imperfect macromixing and partial segregation in a stirred semi-batch reactor. *Chem Eng Sci.* 1992;47:2825-2830.
12. Doraiswamy LK, Sharma MM. *Heterogeneous Reactions. Vol. 2. Fluid–Fluid–Solid Reactions*. New York, NY: Wiley; 1984.
13. Baldyga J, Bourne JR. *Turbulent Mixing and Chemical Reactions*. New York, NY: Wiley; 1999.
14. Shah YT. *Gas–Liquid–Solid Reactor Design*. New York, NY: McGraw-Hill; 1979.
15. Gianetto A, Silveston OL. *Multiphase Chemical Reactors*. Washington, DC: Hemisphere; 1986.
16. Fan L-S. *Gas–Liquid–Solid Fluidization Engineering*. Boston, MA: Butterworth-Heinemann; 1989.
17. Beenackers AACM, van Swaaij WPH. Chemical reactor design and technology. DeLasa HI, ed. NATO Advanced Study Institute Series. Dordrecht, The Netherlands: Martinus Nijhoff; 1986.
18. Krishna R, Ellenberger J. A unified approach to the scale-up of "fluidized" multiphase reactors. *Trans IChemE.* 1995;73(A):217-221.
19. Nigam KDP, Schumpe A, eds. *Three-Phase Sparged Reactors*. New York, NY: Gordon & Breach; 1996.
20. Dudukovic MP, Larachi F, Mills PL. Multiphase reactors—Revisited. *Chem Eng Sci.* 1999;54:1975-1995.
21. Lapin A, Lübbert A. Numerical simulation of the dynamics of two-phase gas–liquid flows in bubble columns. *Chem Eng Sci.* 1994;49: 3661-3674.
22. Delnoij E, Kuipers JAM, van Swaaij WPM. Dynamic simulation of gas–liquid two-phase flow: Effect of column aspect ratio on the flow structure. *Chem Eng Sci.* 1997b;52:1429-1458.
23. Delnoij E, Kuipers JAM, van Swaaij WPM. A three-dimensional CFD model for gas–liquid bubble columns. *Chem Eng Sci.* 1999;54:2217-2226.
24. Lain S, Broder D, Sommerfeld M. Experimental and numerical studies of the hydrodynamics in a bubble column. *Chem Eng Sci.* 1999;54: 4913-4920.
25. Sokolichin A, Eigenberger G. Gas–liquid flow in bubble columns and loop reactors: Part I. Detailed modeling and numerical simulation. *Chem Eng Sci.* 1994;49:5735-5746.
26. Pfleger D, Gomes N, Gilbert H, Wagner H. Hydrodynamic simulations of laboratory scale bubble columns fundamental studies of the Eulerian–Eulerian modeling approach. *Chem Eng Sci.* 1999;54:5091-5099.
27. Pfleger D, Becker S. Modeling and simulation of the dynamic flow behavior in a bubble column. *Chem Eng Sci.* 2001;56:1737-1747.
28. Pan Y, Dudukovic M, Chang M. Numerical investigation of gas-driven flow in 2-D bubble columns. *AIChE J.* 2000;46:434-449.
29. Fox RO. On the relationship between Lagrangian micromixing models and computational fluid dynamics. *Chem Eng Process.* 1998;37:521-535.
30. Khinast JG, Koynov AA, Leib TM. Reactive mass transfer at gas–liquid interfaces: Impact of micro-scale fluid dynamics on yield and selectivity of liquid-phase cyclohexane oxidation. *Chem Eng Sci.* 2003;58:3961-3971.
31. Sundaresan S. Modeling the hydrodynamics of multiphase flow reactors: Current status and challenges. *AIChE J.* 2000;46:1102-1105.
32. Aris R. Mass transfer from small ascending bubbles. *Chem Eng Sci.* 1997;52:4439-4446.
33. Legendre D, Magnaudet J. Effect of flow acceleration on mass or heat transfer at the surface of a spherical bubble. *C R Acad Sci Paris.* 1999;327:63-70.
34. Deen NG, van Sint Annaland M, Kuipers JAM. Multiscale modeling of dispersed gas–liquid two-phase flow. *Chem Eng Sci.* 2004;59:1853-1861.
35. Tokuhiro A, Maekawa M, Iizuka K, Hishida K, Maeda M. Turbulent flow past a bubble and an ellipsoid using shadow-image and PIV techniques. *Int J Multiphase Flow.* 1998;24:1383-1406.
36. Lage PLC, Esposito R. Experimental determination of bubble-size distributions in bubble columns: Prediction of mean bubble diameter and gas hold-up. *Powder Technol.* 1999;101:142-150.
37. Raymond F, Rosant J-M. A numerical and experimental study of the terminal velocity and shape of bubbles in viscous liquids. *Chem Eng Sci.* 2000;55:943-955.

38. Choi HM, Kurihara T, Monji H, Matsui G. Measurement of particle/bubble motion and turbulence around it by hybrid PIV. *Flow Meas Instrum.* 2002;12:421-428.
39. Bork O, Schlueter M, Scheid S, Raebiger N. New phenomena of mass transfer in gas/liquid flows. Proc of ASME HTD, Fluid-physics and heat transfer for macro- and micro-scale gas–liquid and phase change flows, New York; 2001.
40. Bork O, Schlueter M, Scheid S, Raebiger N. Analysis of the effect of local hydrodynamics on mass transfer from bubbles using laser induced fluorescence. Proc of FEDSM'03; 2003:1-7.
41. Scardovelli R, Zaleski S. Direct numerical simulation of free-surface and interfacial flow. *Annu Rev Fluid Mech.* 1999;31:567-603.
42. van Wachem BGM, Schouten JC. Experimental validation of a 3D Lagrangian VOF model: Shape and rise velocity. *AIChE J.* 2002;48:2744-2753.
43. Bothe D, Koebe M, Wielage K, Warnecke H-J. VOF simulations of mass transfer from single bubbles and bubble chains rising in aqueous solutions. Proc of FEDSM'03; 2003:1-7.
44. Shopov PJ, Minev PD, Bazhekov IB, Zapryanov ZD. Interaction of a deformable bubble with a rigid wall at moderate Reynolds numbers. *J Fluid Mech.* 1990;219:241-271.
45. Ryskin GR, Leal LG. Numerical solution of free-boundary problems in fluid-mechanics, Part 1. The finite difference technique. *J Fluid Mech.* 1984a;148:1-17.
46. Ryskin GR, Leal LG. Numerical solution of free-boundary problems in fluid-mechanics, Part 2. Buoyancy driven motion of a gas bubble through a quiescent liquid. *J Fluid Mech.* 1984b;148:19-35.
47. Glimm JW, Grove X, Li L, Oh W, Sharp DH. A critical analysis of Rayleigh–Taylor growth rates. *J Comput Phys.* 2001;169:652-677.
48. Tryggvason G, Bunner B, Esmaeeli A, Juric D, Al-Rawahi N, Tauber W, Han J, Nas S, Jan Y. A front-tracking method for the computations of multiphase flow. *J Comput Phys.* 2001;169:708-759.
49. Sankaranarayanan K, Kevrekidis IG, Sundaresan S, Lu J, Tryggvason G. A comparative study of lattice Boltzmann and front-tracking finite-difference methods for bubble simulations. *Int J Multiphase Flow.* 2003;29:109-116.
50. Reese J, Fan L-S. Hydrodynamics of a bubble column with a conical-shaped entrance region. *Chem Eng Sci.* 1997;52:1553-1559.
51. Tsuchiya K, Furumoto A. Tortuosity of bubble rise path in a liquid–solid fluidized bed: Effect of particle shape. *AIChE J.* 1995;41:1368-1374.
52. Guder R. *Fluidynamik von Dreiphasenströmungen in Treibstrahlschlaufenreaktoren*. Doctoral Dissertation. Bremen, Germany: Universität Bremen; 1997.
53. Fan L-S, Tsuchiya K. *Bubble Wake Dynamics in Liquids and Liquid–Solid Suspensions*. Boston, MA: Butterworth-Heinemann; 1990.
54. Chen YM, Fan L-S. Bubble breakage mechanisms due to collision with a particle in liquid medium. *Chem Eng Sci.* 1989;44:117-132.
55. Brucker C. 3-D scanning particle-image-velocimetry: Technique and application to a spherical cap wake flow. *Appl Sci Res.* 1996;65:157-179.
56. Millies M, Mewes D. Calculation of circulating flows in bubble columns. *Chem Eng Sci.* 1995;50:2093-2106.
57. Brauer H. Turbulenz in mehrphasigen Strömungen. *Chem-Ing-Tech.* 1979;51:934-948.
58. Bhaga D, Weber ME. Bubbles in viscous liquids: Wakes, shapes and velocities. *J Fluid Mech.* 1981;105:61-85.
59. Tse K, Martin T, McFarlane CM, Nienow AW. Visualization of bubble coalescence in a coalescence cell, a stirred tank and a bubble column. *Chem Eng Sci.* 1998;53:4031-4036.
60. Grace JR. Shapes and velocities of bubbles rising in infinite liquids. *Trans IChemE.* 1973;51:116-120.
61. Lee LJ, Fan L-S. In: Furusaki S, Garside J, Fan L-S, eds. *The Expanding World of Chemical Engineering*. Chapter 9. New York, NY: Taylor & Francis; 2002.
62. Bentley BJ, Leal LG. An experimental investigation of drop deformation and breakup in steady, two-dimensional linear flows. *J Fluid Mech.* 1986;167:241-283.
63. Tsouris C, Tavlarides L. Breakage and coalescence models for drops in turbulent dispersions. *AIChE J.* 1994;40:395-406.
64. Bork O, Schlüter M, Scheid S, Räbiger N. New phenomena of mass transfer in gas/liquid flows. Proc of ASME HTD, Fluid-physics and heat transfer for macro- and micro-scale gas–liquid and phase change flows; 2001:1-6.
65. Peskin CS. Numerical analysis of blood flow in the heart. *J Comput Phys.* 1977;25:220-252.
66. Press WH, Flannery BP, Teukolsky SA, Vetterling WT. *Numerical Recipes: The Art of Scientific Computing*. Cambridge, UK: Cambridge Univ. Press; 1989.
67. Redfield JA, Houghton G. Mass transfer and drag coefficients for single bubbles at Reynolds numbers of 0.02–5000. *Chem Eng Sci.* 1995;20:131-139.
68. Ponoth SS, McLaughlin JB. Numerical simulation of mass transfer for bubbles in water. *Chem Eng Sci.* 2000;55:1237-1255.

Manuscript received Aug. 15, 2004, and revision received Feb. 15, 2005.